Surface & Coatings Technology 286 (2016) 49–56

Contents lists available at ScienceDirect

Surface & Coatings Technology

journal homepage: www.elsevier.com/locate/surfcoat

Microstructure characteristics of EB-PVD YSZ thermal barrier coatings corroded by molten volcanic ash

Canying Cai [a,b,*], Sheng Chang [a,b], Yichun Zhou [a,b], Li Yang [a,b], Guangwen Zhou [c], Yanguo Wang [a,b]

[a] School of Materials Science and Engineering, Xiangtan University, Xiangtan 411105, China
[b] Key Laboratory of Low Dimensional Materials &Application Technology of Ministry of Education, Xiangtan University, Xiangtan 411105, China
[c] Department of Mechanical Engineering & Materials Science and Engineering Program, Binghamton University, Binghamton, NY 13902, USA

ARTICLE INFO

Article history:
Received 4 August 2015
Revised 30 November 2015
Accepted in revised form 1 December 2015
Available online 2 December 2015

Keywords:
Corrosion
Microstructure
Thermal barrier coatings
Yttria-stabilized zirconia

ABSTRACT

Y_2O_3-stabilized ZrO_2 (YSZ) thermal barrier coatings (TBCs) grown on a polycrystalline alumina (Al_2O_3) substrate are corroded by a natural volcanic ash (VA) at 1150 °C. The VA corrosion-induced microstructure development and composition evolution across the YSZ coating layer and at the VA/YSZ and YSZ/Al_2O_3 interfaces are investigated by scanning electron microscopy (SEM), X-ray diffraction (XRD), Raman spectroscopy, energy-dispersive X-ray spectroscopy (EDS) and transmission electron microscopy (TEM). It is found that the VA-corroded YSZ coating undergoes grain growth and becomes well-connected along the deposition direction. It is shown that VA-molten depositions penetrate through the entire YSZ layer and fully fill the intercolumnar gaps in the YSZ layer, which results in crystalline $ZrSiO_4$ precipitates between the intercolumnar gaps near the VA/YSZ interface and anorthite ($CaAl_2Si_2O_8$) precipitates at the YSZ/Al_2O_3 interface with the micro-crack formation. The growth stresses associated with the anorthite precipitation is suggested as the driving force to initiate the degradation of TBCs at the YSZ/Al_2O_3 interface region.

1. Introduction

Thermal barrier coatings (TBCs) are extensively used to protect metallic components of aircraft engines operated in an aggressive environment for improving the engine efficiency by increasing the operating temperatures [1–7]. TBCs generally consist of an yttria-stabilized zirconia coating deposited onto an oxidation-resistant bond-coat alloy. Typically, the presence of a segmented and porous 7 wt.% (4 mol%) Y_2O_3-stabilized ZrO_2 ceramic coating contributes strongly to the thermal barrier function and strain tolerance [8]. There are two main types of commercial TBCs used in aircraft engines. One is deposited typically on rotating parts by electron-beam physical vapor deposition (EB-PVD) with columnar grains normal to the coating/substrate interface and the intercolumnar porosity. The other is deposited typically on stationary components by the low-cost process of air plasma spray (APS) with porosity generally parallel to the interface [3–4].

Increasing the turbine inlet temperature has engendered a new failure for a jet plane flying through air contaminated with siliceous minerals (dust, sand, and volcanic ash) consisting of calcium-magnesium-alumina-silicates (CMAS), which are ingested with the intake air and deposited on the hot surface of the engine components [9–19]. The CMAS ash can melt in the engine to form molten glass. The reaction between molten CMAS and the YSZ coating can lead to significant changes in the morphology, microstructure, and composition of the YSZ coating and result in degradation of the TBCs [20–23]. The intercolumnar porosity structure of EB-PVD TBCs makes it susceptible to this type of attack. Corrosion is prone to occur when the TBCs are exposed to volcanic ash (VA) since VA has a melting temperature, ranging from 1090 °C to 1150 °C, lower than the temperatures in the combustion chamber of a jet engine, in excess of 1600 °C [24]. It has been shown that VA acts as a solvent for Y_2O_3 and reacts with ZrO_2 to form $ZrSiO_4$ at the expense of YSZ [25]. Significant advances in understanding the microscopic processes leading to the TBCs failure have been made, including the thermo-mechanical interactions and the thermo-chemical interactions [26–29]. However, there is still a key challenge in understanding the thermo-chemical interaction due to variations in the amount and chemical composition of the molten glass formed on the coating surface [29]. Moreover, the VA attack process takes place under highly dynamic conditions with strong temperature, compositional, and chemical gradients. Therefore, detailed characterization of the corrosion feature in the bulk of the YSZ layer and at the VA/YSZ and YSZ/TGO (TGO: thermally grown aluminum oxide) interfaces is necessary for developing an improved understanding of the thermo-chemical interactions between TBC materials and the molten VA, which is essential for elucidating the VA-corrosion induced failure phenomena in TBCs.

Mechnich et al. studied the chemical interaction and the microstructure development of the YSZ coating corroded by artificial volcanic

* Corresponding author at: School of Materials Science and Engineering, Xiangtan University, Xiangtan 411105, China.
E-mail address: cycai@xtu.edu.cn (C. Cai).

http://dx.doi.org/10.1016/j.surfcoat.2015.12.003
0257-8972/

ash (AVA) matching the bulk composition of the April 15, 2010 Eyjafjallajokull (Iceland) volcanic eruption within relatively short reaction time (1 h only) and showed that VA can penetrate the top part of the YSZ layer [25]. However, information regarding the corrosion characterizations of the entire YSZ layer and the YSZ/TGO interface induced by prolonged VA corrosion at high temperatures is still lacking. Detailed investigations on the corrosion feature of the entire TBC system will provide mechanistic insight into understanding the failure mechanism of TBCs under operating conditions. Furthermore, the interaction process between VA and YSZ may be different even if the same corrosion conditions are taken owing to variations in the chemical composition of VA from different areas [25]. In the present work, the TBC system is progressively corroded by a VA collected from Sakurajima volcano in Japan (eruption date: 10th March, 2009). The VA-corrosion induced phase evolution and morphological development at the VA/YSZ interface, across the entire YSZ layer and at YSZ/TGO interfaces are studied in detail by means of scanning electron microscopy (SEM), X-ray diffraction (XRD), Raman spectroscopy, energy-dispersive X-ray spectroscopy (EDS) and transmission electron microscopy (TEM).

2. Materials and methods

To assess the potential effect of the molten VA on YSZ and TGO and avoid the complexity associated with excessive oxidation and microstructure degradation of the NiAl-based bonding coating during isothermal VA corrosion, an alumina substrate is used as a substitute for the superalloy substrate of the bonding coating in the present work. A 100-μm thick TBC layer of 7 wt.% Y_2O_3 partially stabilized ZrO_2 is deposited on an alumina (98% purity) substrate via an electron-beam physical vapor deposition (EB-PVD) system (UE-204B). The alumina substrate is held at 900 °C with a rotation rate of 25 rpm (rotation per min) to achieve the characteristic columnar structure of the YSZ coating.

Composition of the VA is dominated by SiO_2 content as shown in Table 1. A fine powder of the VA is made by ball-milling, and then screened by an 800-mesh sieve. Grain size of the fine powder is determined using a particle-size analyzer (Mastersizer 2000, Malvern Instruments, UK). As shown in Fig. 1(a), the as-prepared VA powder shows a continuous grain size distributing from 0.1 μm to 20 μm and a d_{50} (i.e. 50% of grains) value is approximately 5 μm. Thermal properties of the VA up to 1300 °C are determined using differential scanning calorimetry (DSC, STA 449, Netzsch, Germany), at a heating rate of 20 °C/min. The DSC plot shown in Fig. 1(b) reveals two major thermal effects. An endothermic phase transition is evident between 900 °C and 950 °C. The VA consists of glassy phases owing to rapid quenching from its melt state. The endothermic transition between 900 °C and 950 °C is related to the glass transition. A second significant endothermic reaction with a very broad peak around 1180 °C implies that there exists a melting temperature range, owing to the large content of glass-state silica in the VA. The characterization by XRD indicates that the as-prepared VA is dominated by non-crystalline constituents with minor crystalline constituents such as feldspar, pyroxene and olivine.

A thick paste of the VA is made by mixing the fine powders with ethanol (1 mg VA/0.01 ml ethanol) and subsequently painted to the surface of the YSZ with an area density of about 10 mg/cm^2. These specimens are placed on an alumina plate with the VA-deposited surface facing up. High temperature corrosion experiment of the TBC specimens with the VA depositions is performed in a muffle furnace at 1150 °C for 4 h, 12 h, and 24 h, respectively. The heating and cooling rates both are 10 °C/min.

Metallographic samples of the as-deposited TBCs and VA-corroded TBCs are prepared by embedding in epoxy and subsequently cutting into slices along the direction parallel to the growth direction of the TBCs in order to avoid coating spallation. These slices are polished successively using 2000 grit and 3000 grit SiC paper. A layer of platinum (Pt) is plated on the polished surface to obtain clear SEM images. SEM (Qunanta FEG-250, FEI) is used to characterize the microstructure and composition. The morphology images are obtained by collecting the backscattered electrons.

XRD analyses are performed with a D/MAX 2500 diffractometer using Cu Kα radiation. XRD patterns are obtained from the top surface layer, the middle layer (~50 μm down from the top surface) and the interface layer (~100 μm down from the top surface), respectively. Raman Spectra are characterized using a Renishaw Invia laser Raman Spectrometer from the top surface layer (~5 μm down from the top surface) and the interface layer (~100 μm down from the top surface). The different coating depths are obtained by wearing off the YSZ coating with a mechanical mill to each pre-defined thickness measured by a micrometer.

Cross-sectional TEM samples are prepared following the procedure proposed by P. Poza et al. [30]. Firstly, the samples are cut in half along the thickness direction and the top surfaces are struck together using Bond 610 glue after cleaning. The samples are then mechanically thinned successively using SiC paper with increasingly fine grits to about 60 μm thickness, where 3500 grit SiC papers are finally used. A Fischione Model 200 dimpling grinder is used to dimple the thinned sample to about 10 μm. Finally, a Fischione Model 200 ion milling is used for further thinning. The prepared TEM samples are characterized using a JEM-2100 TEM.

3. Results and discussion

3.1. Microstructure characterization of VA-corroded TBCs

3.1.1. SEM characterization

Fig. 2 shows representative cross-sectional SEM morphology images of the as-prepared and VA-corroded samples. As a reference, Fig. 2(a) is a typical SEM image of the as-deposited EB-PVD TBCs on the Al_2O_3 substrate, which shows that the YSZ layer is about 100 μm thick and is adherent to the A_2O_3 substrate. As shown in the inset zoomed-in SEM image in the lower right corner of Fig. 2(a), the YSZ layer has a columnar structure with the columnar grains perpendicular to the YSZ/Al_2O_3 interface. It can also be noted that the YSZ coating shows wavy layers (as indicated by the black broken lines) roughly parallel to the YSZ/Al_2O_3 interface. The SEM image also shows there are intercolumnar gaps in the YSZ layer (as indicated by the black arrows). Fig. 2(b–d) are typical SEM morphology images of the samples corroded by molten VA at 1150 °C for 4 h, 12 h, and 24 h, respectively. As seen in Fig. 2(b), the VA completely wets the top YSZ layer and there is no physical gap at the VA/YSZ interface area for the sample corroded for 4 h, indicating that the VA layer becomes molten after the corrosion for 4 h. No other significant differences in the morphological features can be noted in the 4-h corroded sample compared to the as-deposited YSZ sample. For instance, the YSZ coating still remains its columnar structure with

Table 1
Chemical compositions of VA materials from this study as compared to Iceland.

Vakyes in (mol% or wt.%)	SiO_2	Al_2O_3	CaO	MgO	FeO	TiO_2	Na_2O	K_2O	Traces
Iceland Volcanic ash (wt.%)	57.69	15.48	5.15	2.15	9.61	1.59	5.25	1.72	1.36
Volcanic ash* (wt.%)	54.90	12.48	10.34	3.04	13.11	–	4.25	1.72	0.26
Volcanic ash* (mol%)	58.33	7.69	11.54	5.13	11.54	–	4.49	1.28	–

* Used in this work, location of eruption: Sakurajima volcano, eruption date: 10th March, 2009, location of collection; Furusato hot spring.

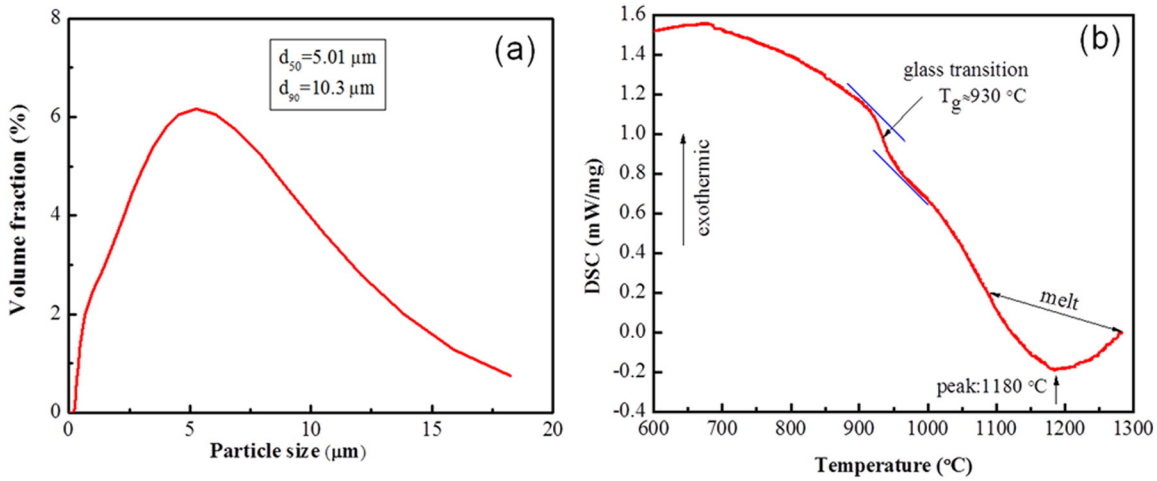

Fig. 1. (a) Particle size distribution of the VA after ball milling.; (b) differential scanning calorimetry (DSC) profile of the VA in the temperature ranging from 500 °C to 1280 °C. Note the sigmoidal glass transition occurs at approximately 930 °C and there exists a melting temperature range around 1180 °C.

the wavy layered feature (as indicated by black broken lines) and the average size of the columnar grains does not show appreciable difference from the un-corroded sample. With increasing the corrosion time up to 12 h and 24 h, the columnar grains become well connected along the vertical direction as shown in Fig. 2(c–d). Moreover, the columnar grains have increased aspect ratios of length to diameter as shown in the zoomed-in SEM image in Fig. 2d. Fig. 2(c–d) also show that the initial wavy layer feature of the YSZ layer disappears, which may be related to the curvature effect, where the convex portions of the YSZ may have a faster corrosion rate than the concave portions. In addition, Fig. 2(b-d) also show that the VA-corroded YSZ coating layers still remain adherent to the Al_2O_3 substrate for the different corrosion durations.

To determine the level of VA infiltration, the time-dependent spatial distribution of silicon in the corroded samples is qualitatively analyzed by EDS elemental mapping since the composition of the VA is dominated by SiO_2. Fig. 3(a–c) show the Si mapping images of the samples corroded by molten VA at 1150 °C for 4 h, 12 h, and 24 h, respectively. For the sample corroded for 4 h, most of the Si intensity is located at the top surface layer although there is some weak Si signal across the entire YSZ layer (Fig. 3(a)). With increasing the corrosion time, the intensity of Si signal increases across the entire YSZ coating layer.

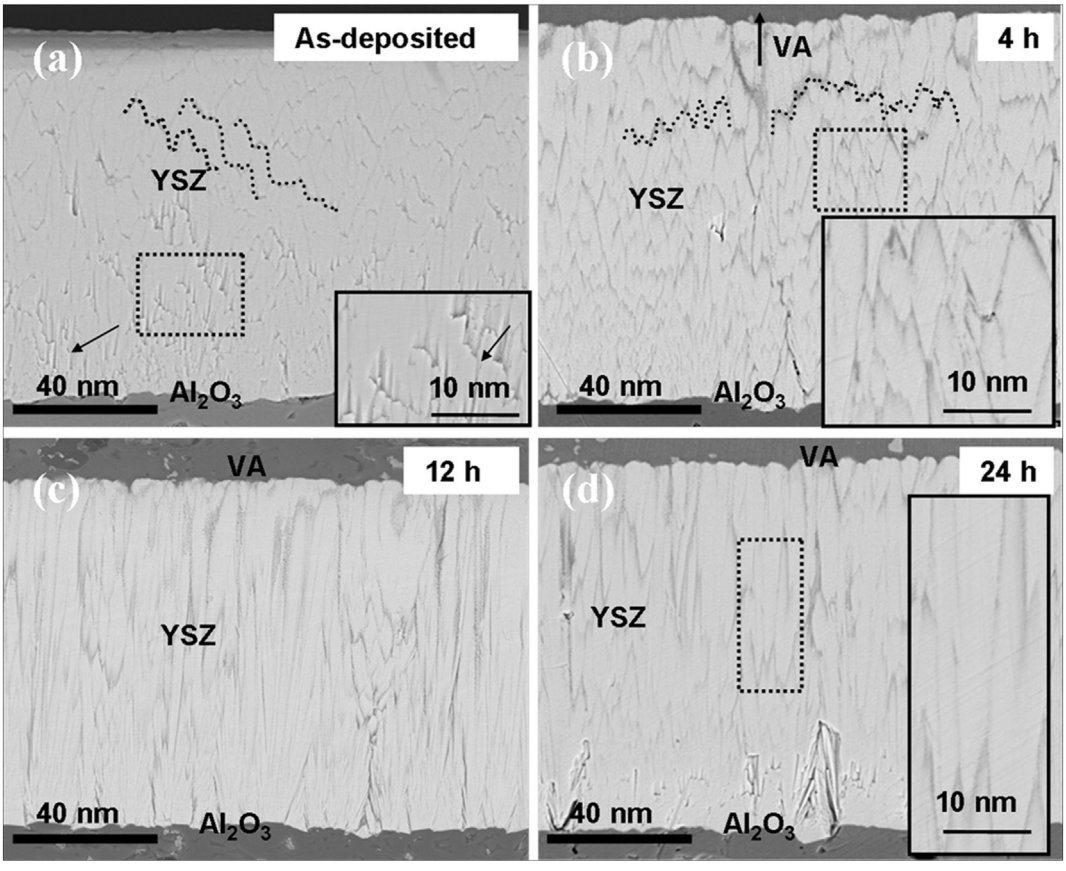

Fig. 2. Cross-sectional SEM morphology images of the as-sprayed sample (a) and the VA-corroded samples at 1150 °C for 4 h (b); 12 h (c); 24 h (d).

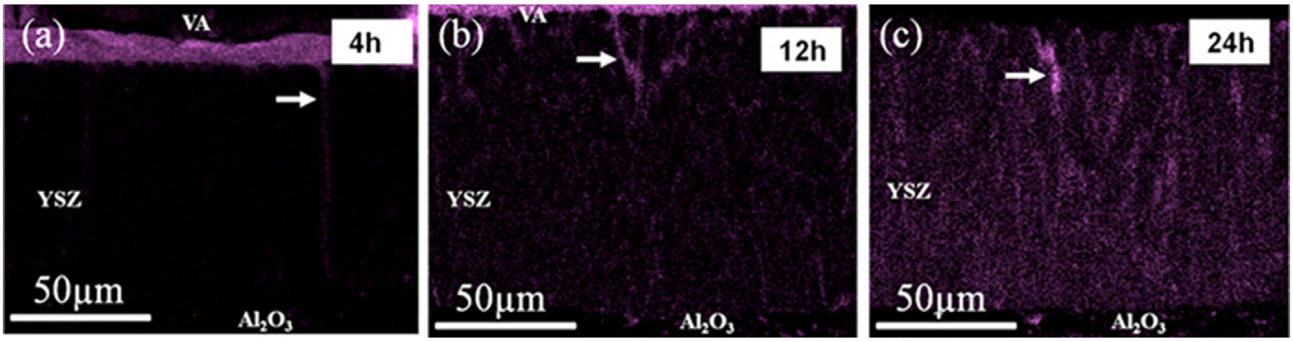

Fig. 3. Si mapping images of the samples corroded by molten VA at 1150 °C for 4 h (a); 12 h (b); 24 h (c).

This indicates that Si has penetrated through the entire YSZ layer and the quantity of Si in the YSZ layer increases with the duration of corrosion process. From Fig. 3(a–c), one can note that the inter-columnar gaps (marked by white arrows) have more Si intensity than the surrounding grains, indicating that VA infiltrates preferentially through the gaps between columnar grains. These EDS mappings demonstrate that molten VA has already penetrated through the entire YSZ layer and reached the Al_2O_3 substrate for the three samples. Particularly, Fig. 3(c) shows that there is no concentrated Si signal near the surface region, indicating that the molten VA has completely diffused into the YSZ layer.

3.1.2. XRD and Raman spectrums characterization

To complement the SEM analysis on the corrosion-induced morphological and composition evolution, the VA-corroded samples are characterized by XRD. Fig. 4(a) shows XRD patterns of the samples corroded for 4 h, 12 h, and 24 h, respectively. For comparison, an XRD pattern obtained from the as-deposited YSZ sample is also included in Fig. 4(a). It can be seen from Fig. 4(a) that the as-deposited YSZ layer mainly consists of c-ZrO_2 (Fm3m space group, a = 0.513 nm) with minor t-ZrO_2 (P42/nmc space group, a = 0.364 nm and c = 0.527 nm). It can be noted that the (200) peak shows much stronger intensity than the (111) peak, suggesting that the sample has a (200) textured structure. After the VA-corrosion for 4 h, some new diffraction peaks associated with $ZrSiO_4$ (I41/amd,a_0 = 0.659 nm,b_0 = 0.594 nm) become visible. The $ZrSiO_4$ phase is also found for the 12-h corroded and 24-h corroded samples. The zoomed-in XRD peak at about 35° in the upper-right corner of Fig. 4(a) shows more clearly the gradual increase of the t-ZrO_2 and $ZrSiO_4$ phases in the samples corroded for 4 h, 12 h, and 24 h. Fig. 4(b) displays depth-resolved XRD patterns obtained from the sample corroded for 24 h, where the depths of 0 μm, −50 μm and −100 μm correspond to the coating surface, the middle of the YSZ layer, and the YSZ/Al_2O_3 interface, respectively. It can be seen that the corroded sample remains c-ZrO_2 and t-ZrO_2 in the middle of the coating. However, there is a significant presence of $ZrSiO_4$ at the top surface and of α-Al_2O_3 at the YSZ/Al_2O_3 interface. The α-Al_2O_3 phase at the YSZ/Al_2O_3 interface may come from the alumina substrate. Therefore, the above XRD analyses reveal that VA has reacted with the YSZ to form $ZrSiO_4$ at the surface region. The XRD analyses also indicate that there is no monoclinic zirconia (*m*-ZrO_2) formation in the VA-corroded samples, which was found in the TBC system with CMAS corrosion [21].

When TBCs are corroded, the formation of *m*-ZrO_2 is often considered as one of the key factors leading to the coating failure since the t-ZrO_2 → m-ZrO_2 transformation is accompanied by 3–5% volume expansion [31–32]. However, if there is low amount of m-ZrO_2 in the TBC system, it may not be detected by XRD analysis. In order to further confirm the absence of the m-ZrO_2 phase in the VA-corroded samples, the samples are characterized by Raman spectroscopy since it is more sensitive than XRD for detecting m-ZrO_2. Fig. 5 shows the Raman spectra obtained from the sample that is corroded at 1150 °C for 24 h, where the spectra are taken from the top ceramic layer (YSZ) and the YSZ/Al_2O_3 interface, respectively. For comparison, the standard Raman spectra of m-ZrO_2 and t-ZrO2 are also included in Fig. 5. It can be seen from the spectra that the VA-corroded sample shows a typical Raman spectrum peak of t-ZrO_2 at about 280 cm^{-1} and there is no presence of the characteristic peak around 200 cm^{-1} of m-ZrO_2 as marked in Fig. 5 [21]. The c-ZrO_2 is not characterized by Raman spectra since its Raman spectral pattern is not particularly distinct (only a board peak at about 530–670 cm^{-1})

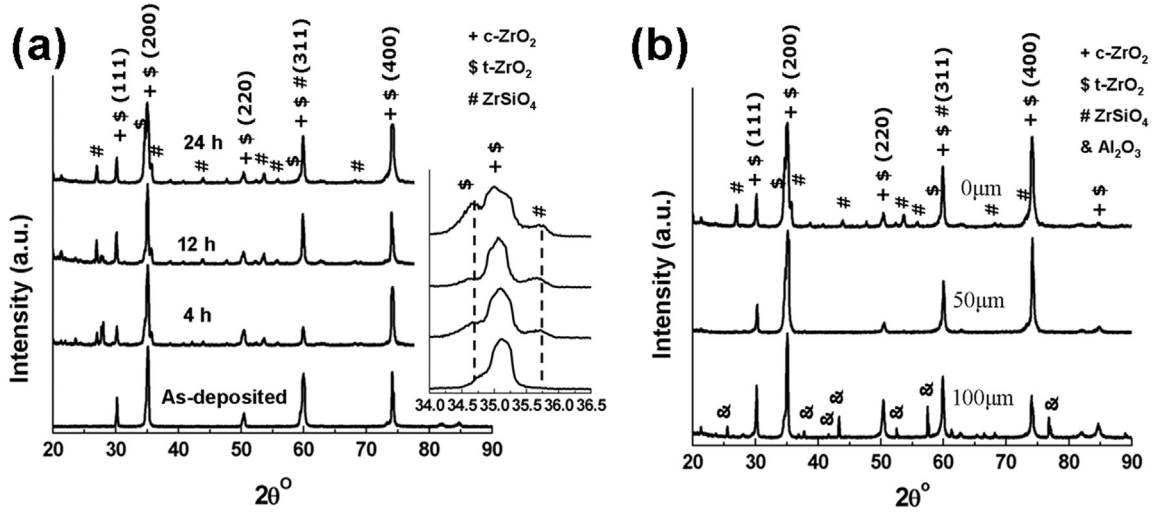

Fig. 4. (a) XRD patterns of the as-deposited YSZ and the YSZ sample corroded by molten VA at 1150 °C for 4 h, 12 h and 24 h, respectively; (b) depth-resolved XRD patterns obtained from the sample corroded for 24 h, where the depths of 0 μm, −50 μm and −100 μm correspond to the coating surface, the middle of the YSZ layer, and the YSZ/Al_2O_3 interface, respectively.

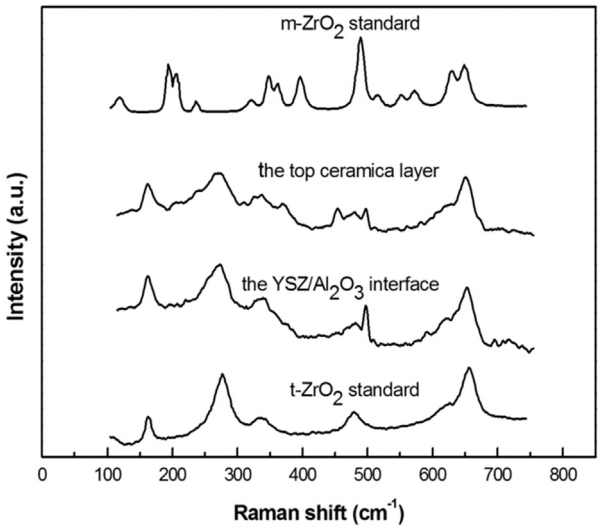

Fig. 5. Raman Spectra of the sample corroded by molten VA at 1150 °C for 24 h, where the spectra are taken from the top ceramic layer (YSZ) in the regions about 5 μm down from the surface and the YSZ/Al_2O_3 interface, respectively; and the standard Raman Spectra of m-ZrO_2 and t-ZrO2 are also included for comparison.

[33]. Therefore, the Raman spectroscopy results further confirm that there is no destructive m-ZrO_2 phase in the corroded TBCs although the YSZ layer obviously displays densification and morphological changes as observed from the SEM characterization (in Fig. 2).

3.1.3. TEM characterization

In order to further reveal the feature of the VA-corrosion induced microstructure development in the TBC layer, the as-deposited and VA-corroded samples are examined by TEM. Fig. 6(a) displays a bright-field (BF) TEM image of the as-deposited sample. The columnar grains in the YSZ layer have the characteristic "feathery" structure, similar to that previously described in the literature [34]. Insert in Fig. 6(a) is a selected area electron diffraction (SAED) pattern taken from the marked white square region, which can be well-indexed with the c-ZrO_2 structure [30]. EDS analysis of the YSZ layer shows that the Y:Zr atomic ratio is about 10.00:90.00 as shown in Table 2.

Fig. 6(b) displays a typical BF TEM image from the middle region of the YSZ coating corroded with VA for 24 h. Comparing with the as-deposited sample, it can be seen that the characteristic "feathery" structures at the tips of the YSZ columnar grains disappeared. Meanwhile, the intercolumnar gaps are now fully filled by VA deposits, which show much brighter contrast than the surrounding YSZ columnar grains. EDS analyses of these bright depositions as marked by a black arrow in Fig. 6(b) show that the depositions mainly consist of Si, Al and Ca (Table 2). The Si content is a little lower while the Al content is slightly higher than those of the un-reacted VA. The SAED (inset of Fig. 6(b)) obtained from the bright deposition regions marked by the black arrow produces diffuse ring diffraction patterns, confirming that the VA depositions remain amorphous. The EDS analysis indicates that the Y:Zr atomic ratio in the YSZ region marked by a white square in Fig. 6(b) is about 9.20:90.80, (Table 2), indicating a slight decrease in the Y content compared with the as-prepared YSZ.

Fig. 6(c) shows a BF TEM image taken from the surface region of the YSZ coating. The ceramic layer is corroded with the formation of VA depositions in the intercolumnar gaps. EDS analysis of the top layer of the YSZ coating (as marked by a white square in Fig. 6(c)) gives a Y:Zr ratio of ~10.70:89.30 as shown in Table 2, which is almost the same as that of the as-prepared YSZ. EDS composition analysis of the bright deposition (at the top layer of YSZ) marked by the black star in Fig. 6(c) shows the presence of Si, Al, Ca, Mg and a little Fe as shown in Table 2, where the Si and Al contents are higher than the other elements, while the Ca and Mg contents are lower than those of the original VA. The SAED of the bright deposition regions reveals the typical diffuse rings for an amorphous material (the SAED pattern is not displayed here). In addition, the SAED analyses reveal the presence of the $ZrSiO_4$ phase with a lateral size of over 1000 nm in between columnar gaps. Inset is an SAED of the $ZrSiO_4$ phase obtained from the region marked by a black circle shown in Fig. 6(c). Indexing of the diffraction pattern matches well with the crystal structure of $ZrSiO_4$. This is in accordance with the XRD data, which shows the significant presence of $ZrSiO_4$ in the surface region of the corroded sample (i.e., Fig. 4(b)).

Fig. 7 shows BF TEM images from the interface region between the YSZ layer and the Al_2O_3 substrate. It can be seen that the original columnar grain structure in the YSZ ceramic layer has transformed into a particulate morphology with significant voids in the YSZ bottom layer and gaps at the YSZ/Al_2O_3 interface, which are filled with VA depositions. EDS analysis of the area marked by a white square shows that the Y:Zr atomic ratio at the YSZ/Al_2O_3 interface is 13.68:82.25 (Table 2), indicating an increase of the Y content compared with the as-deposited YSZ sample. EDS analyses show that the region marked by the white triangle in Fig. 7 mainly consists of Al_2O_3 with the presence of Si and Ca, while the white-circle marked region only consists of Al_2O_3. It can be noted from the EDS analysis that the bright-contrast VA-deposition region (at the YSZ/Al_2O_3 interface marked by a black arrow) mainly consists of Si, Al, Ca (Table 2), where the Si content is lower while Al and Ca contents are higher than those of the un-reacted VA. Moreover, the Si:Al:Ca

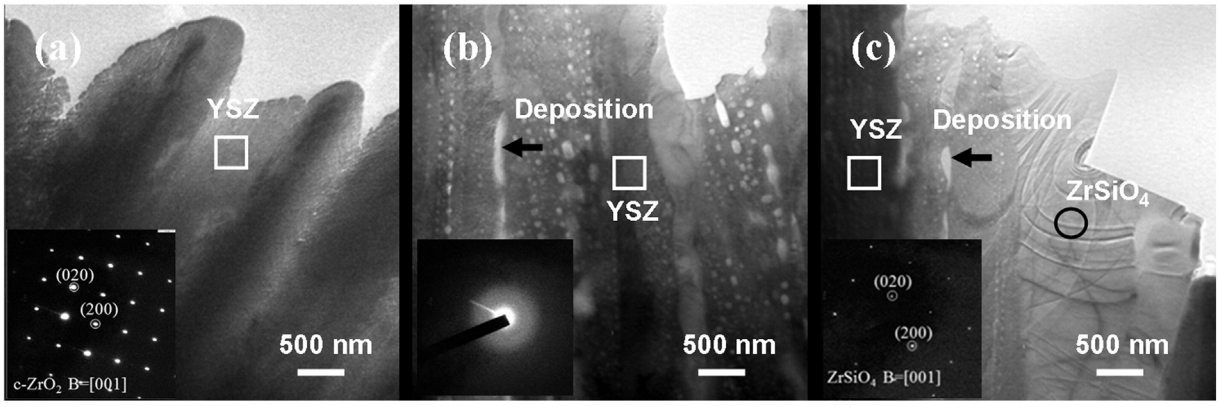

Fig. 6. (a) BF TEM image of the as-deposited sample, where a SAED taken from the white square region confirms that the as-deposited YSZ mainly consists of the cubic structure; (b) BF TEM image from the middle region of the sample corroded with VA at 1150 °C for 24 h, where a SAED obtained from the bright deposition marked by a black arrow confirms that the VA depositions remain amorphous; (c) BF TEM image from the surface region of the YSZ coating, where a SAED obtained from the region marked by a black circle reveals the presence of the $ZrSiO_4$ phase formed in between columnar gaps.

Table 2
Chemical compositions of constituents in the regions of the interacting TBC–VA system. Values are given in mol%.

Region	Constituent (mol%)	SiO_2	$AlO_{1.5}$	CaO	MgO	FeO	$NaO_{0.5}$	$KO_{0.5}$	$YO_{1.5}$	ZrO_2
Original	VA	51.41	13.56	10.17	4.52	10.17	7.90	2.26		
As-deposited	Zirconia								10.0	90.0
Top layer of YSZ	Deposition	70.10	21.32	4.08	3.30	1.21				
Top layer of YSZ	Zirconia								10.70	89.30
Middle layer of YSZ	Deposition	52.47	35.05	12.47						
Middle layer of YSZ	Zirconia								9.20	90.80
YSZ/Al_2O_3 interface	Deposition	43.15	38.88	17.80		0.17				
YSZ/Al_2O_3 interface	Zirconia								13.68	82.25

atomic ratio is close to that of $CaAl_2Si_2O_8$. Inset is an SAED pattern from the bright deposition marked by the black arrow, which can be indexed well with the crystal structure of $CaAl_2Si_2O_8$ (named anorthite). The anorthite phase is not observed in the XRD patterns as shown in Fig. 4, probably due to the small amount of the anorthite phase formed in the YSZ/Al_2O_3 interface region. In addition, it is noted that there is a long and multiple-segmented crack formed in this interface region. The consecutive TEM images shown in Fig. 7(a–c) are taken along the propagation path of the crack. It can be seen that the crack starts from the anorthite region at the YSZ/Al_2O_3 interface (Fig. 7(a)), and then propagates into the alumina substrate along the Al_2O_3 grain boundary (Fig. 7(b)), and ends in the Al_2O_3 substrate (Fig. 7(c)). Fig. 7(c) also shows that there is VA deposition at the end of the crack, suggesting that molten VA diffuses through the long crack and becomes internal precipitates inside the alumina substrate. The observed anorthite precipitate at the end of the crack also serves as clear evidence that the crack is a real microstructure feature induced by the anorthite formation rather than an artifact from the TEM specimen preparation process. This observation also reveals that the crack generated by anorthite precipitates can propagate progressively for a long path (> several μm) along the grain boundary in the alumina substrate, which may initiate the spallation at the YSZ/Al_2O_3

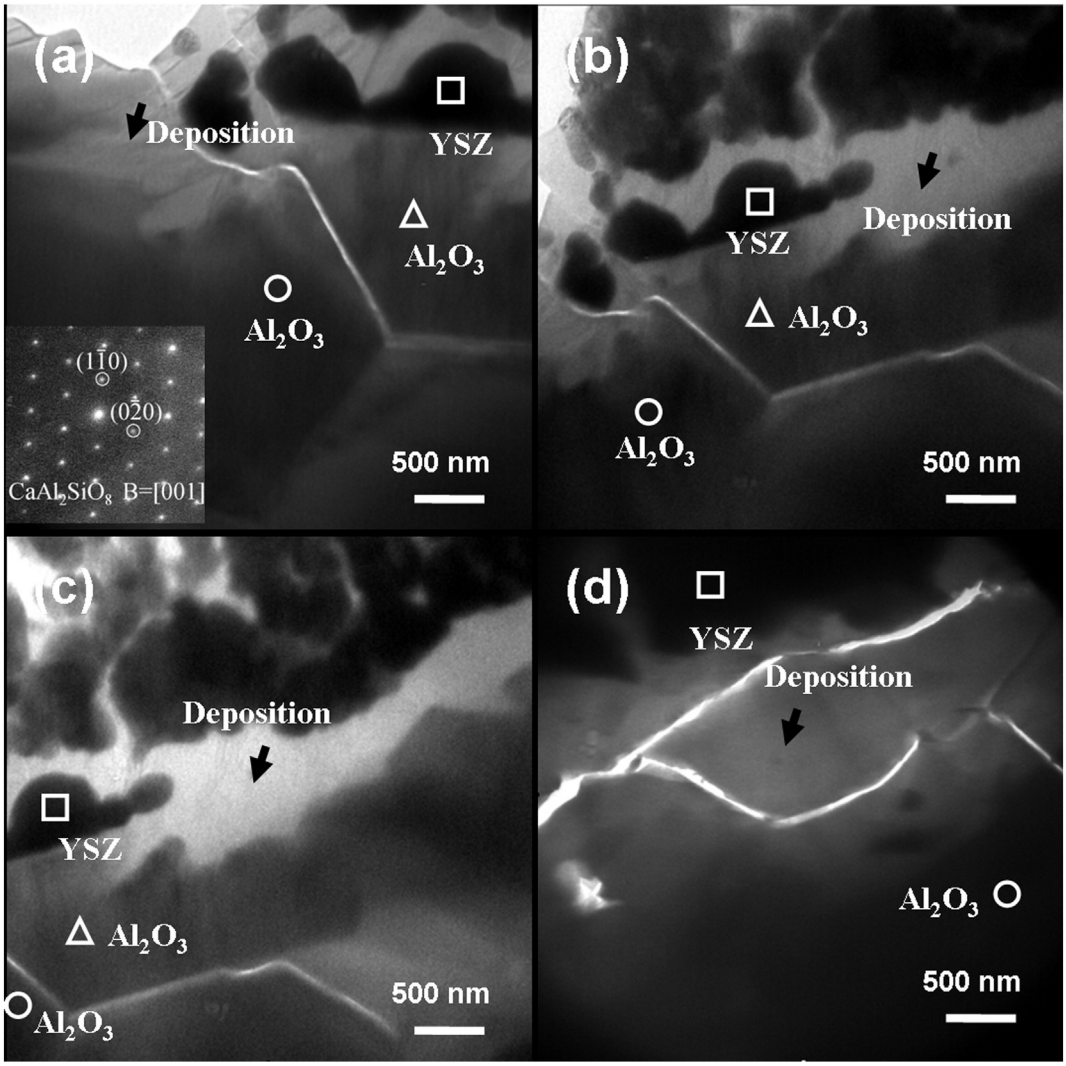

Fig. 7. BF TEM images taken from the interface region between the YSZ layer and the Al_2O_3 substrate, where an SAED pattern from the bright deposition as marked by the black arrow is indexed well with the crystal structure of $CaAl_2Si_2O_8$: (a–c) showing the consecutive propagation path of the crack; (d) similar cracks are observed in another region with anorthite precipitate.

interface and thus the failure of the TBCs. This is further confirmed by the presence of similar cracks associated with anorthite precipitates in other regions as shown in Fig. 7(d).

3.2. Discussion

When the TBCs are corroded by the molten VA, columnar grains undergo grain growth at the high temperature, which results in well-connected columnar grains along the YSZ deposition direction. Meanwhile, the molten VA infiltrates the YSZ layer through the gaps between columnar grains. $ZrSiO_4$ forms in the top of the YSZ, while anorthite ($CaAl_2Si_2O_8$) forms in the YSZ/Al_2O_3 interface region. The different corrosion features along the YSZ thickness direction may be related to their local chemical environments.

Fig. 8(a) is a schematic summary of the microstructure feature of the VA-corroded YSZ. $ZrSiO_4$ forms at the top surface of the ceramic layer. The reaction in the binary ZrO_2–SiO_2 system is sluggish at the present corrosion temperature (1150°) [35]. $ZrSiO_4$ formation observed here may be related to the Y-rich environments [25]. The Y:Zr atomic ratios in the corroded YSZ layer are higher than that of the as-deposited sample as shown in Table 2. The increasing Y content indicates that VA corrosion may induce Y-enrichment around the intercolumnar gaps. On the other hand, the compositions of the VA depositions depend on the VA infiltration depth along the corroded YSZ layer as shown in Table 2. The Si content is higher than the original VA at the top ceramic. From the top surface through the YSZ layer to the YSZ/Al_2O_3 interface, the Si content decreases gradually, indicating that Si mainly enriches at the top ceramic. During VA corrosion, Y_2O_3 (that forms solid solution with ZrO_2) in the YSZ layer may be dissolved into the molten VA. The Y_2O_3-rich environment in the molten VA may enhance the chemical interaction between ZrO_2 and SiO_2. As a result, the reaction of Zr-Si-O in the molten VA leads to the precipitation of $ZrSiO_4$ at the top of the ceramic layer at 1150 °C.

In the YSZ/Al_2O_3 interface region, a new phase, anorthite ($CaAl_2Si_2O_8$), is formed, as schematically shown in Fig. 8(a). The anorthite formation can be related to the Al-rich and Ca-rich environment in the interface region. As shown in Table 2, both the Al and Ca contents increase from the surface region to the YSZ/Al_2O_3 interface and reach the maximum at the YSZ/Al_2O_3 interface region. The Al content in the YSZ/Al_2O_3 interface is higher than that of the original VA. Both Al-rich and Ca-rich environments are mandatory for the anorthite formation [21,36], which can be obtained at the YSZ/Al_2O_3 interface due to the supply of Al from the alumina substrate. Therefore, the VA remains an amorphous state in the top surface and in the middle of the YSZ layer, while the mixture of CaO and SiO_2 in the molten VA arriving at the YSZ/Al_2O_3 interface reacts with the alumina substrate to form anorthite in the YSZ/Al_2O_3 interface region.

As shown in Fig. 8(b), a crack appears in the anorthite region of the YSZ/Al_2O_3 interface and propagates along the grain boundary in the Al_2O_3 substrate. The crack may be mainly caused by the growth stress of anorthite that precipitates at the YSZ/Al_2O_3 interface due to the Al-rich environment there. The anorthite growth requires the supply of Ca and Si from the molten VA and Al from the alumina substrate. By considering the difference in the specific densities of anorthite (2.6–2.76 g/cm^3), VA (2.69 g/cm^3) [37], the formation of the anorthite phase in the interface region is accompanied with a volume expansion that results in compressive stresses in the anorthite precipitates and at the YSZ/Al_2O_3 due to their molar volume mismatch, which may drive the formation of cracks in the interface region. On the other hand, the thermal expansion coefficient of anorthite (5.0 ppm/°C) is smaller than those of ZrO_2 (11.0 ppm/°C) and Al_2O_3 (8.0 ppm/°C). Their thermal expansion mismatch also induces the thermal stress in the interface region during TBCs cooling. However, as shown in Fig. 7(c), it can be seen that some anorthite depositions have penetrated and gathered at the end of the crack, indicating that the crack has already formed at the high temperature and its formation is caused by the growth stresses, rather than the thermal stress. Therefore, VA-penetration induced anorthite formation has deleterious effects on the durability of the TBCs, which may potentially lead to the YSZ/Al_2O_3 interfacial delamination as a result of the growth stresses accumulated at the interfacial area. The YSZ/TGO interfacial failure observed from our experiments is caused by the thermo/chemo-mechanical coupling effects. While we do not have a practical way to overcome this interfacial cracking issue, depositing an extra coating capable of resisting the VA infiltration may be an option as suggested by Drexler et al. [38].

4. Conclusion

In summary, the microstructure and composition evolution of the VA-corroded YSZ is studied in detail on the basis of SEM, XRD, TEM and Raman spectroscopy data. It is found that the VA penetrates through the entire YSZ layer and further infiltrates into the alumina substrate. The VA-penetration induced depth-dependent chemical environment in the YSZ layer results in the depth-dependent reaction products: $ZrSiO_4$ forms near the top surface region of the YSZ layer owing to its Y_2O_3-rich environment, amorphous VA fully fills the intercolumnar gaps in the middle of the YSZ layer. The anorthite phase precipitates around the YSZ/Al_2O_3 interface region due to the

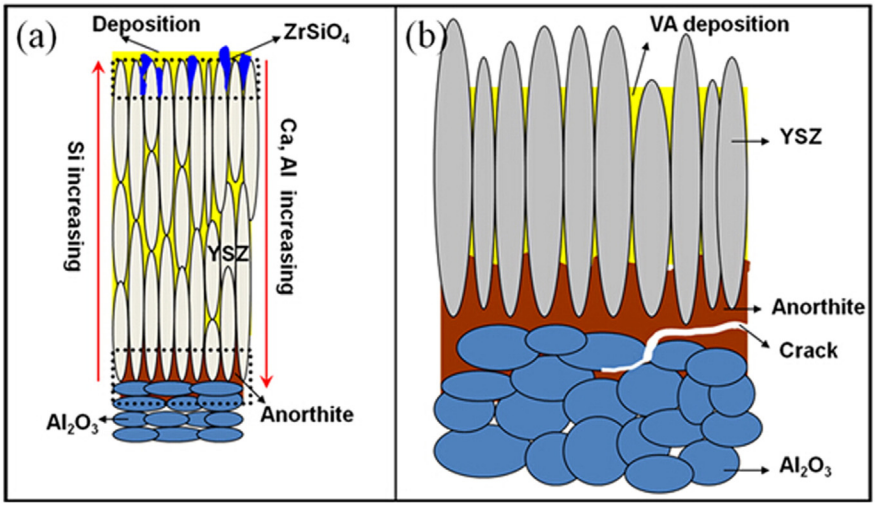

Fig. 8. (a) Schematic illustration of the microstructure feature of the VA-corroded YSZ; (b) Schematic illustration of a crack appearing in the anorthite region near the YSZ/Al_2O_3 interface and propagating along the grain boundary in the alumina substrate.

Al-rich and Ca-rich environments, which are mandatory for anorthite formation. The molar volume mismatch between anorthite, ZrO_2, and Al_2O_3 induces the crack formation that further propagates into the alumina substrate along the Al_2O_3 grain boundaries. The anorthite induced crack formation may initiate the exfoliation of the YSZ coating at the YSZ/Al_2O_3 region. These results provide mechanistic insight into understanding the failure mechanisms of TBCs under service conditions.

Acknowledgments

This work was supported by the National Natural Scientific Foundation of China (Grant Nos. 11274263 and 11274264), the opening project of State Key Laboratory of Explosion Science and Technology (Beijing Institute of Technology, the opening project No. KFJJ15-05M) and "Hundred Talents Program" of Hunan Province, China. The authors acknowledge Rudder Wu for providing the volcanic ash.

References

[1] C.H. Liebert, R.A. Miller, Ceramic thermal barrier coatings, Ind. Eng. Chem. Prod. Res. Dev. 23 (3) (1984) 344–349.
[2] P.K. Wright, A.G. Evans, Mechanisms governing the performance of thermal barrier coatings, Curr. Opin. Solid State Mater. 4 (3) (1999) 255–265.
[3] A.G. Evans, D.R. Mumm, J.W. Hutchinson, G.H. Meier, F.S. Pettit, Mechanisms controlling the durability of thermal barrier coatings, Prog. Mater. Sci. 46 (2001) 505–553.
[4] N.P. Padture, M. Gell, E.H. Jordan, Thermal barrier coating for gas-turbine engine application, Science 296 (2002) 280–284.
[5] C.G. Levi, Emerging materials and processes for thermal barrier system, Curr. Opin. Solid State Mater. 8 (1) (2004) 77–91.
[6] R. Schafrik, R. Sprague, Saga of gas turbine materials, part III, Adv. Mater. Process. 162 (5) (2004) 29–33.
[7] R. Vassen, A. Stuke, D. Stöver, Recent development in the field of thermal barrier coatings, J. Therm. Spray Technol. 18 (2) (2009) 181–186.
[8] Y.C. Zhou, Q.X. Liu, L. Yang, D.J. Wu, W.G. Mao, Failure mechanisms and life prediction of thermal barrier coatings, Acta Mech. Solida Sin. 31 (5) (2010) 504–531.
[9] D.J. de Wet, R. Taylor, F.H. Stott, Corrosion mechanisms of ZrO_2–Y_2O_3 thermal barrier coatings in the presence of molten middle-east sand, J. Phys. IV 3 (1993) 655–663.
[10] J.L. Smialek, F.A. Archer, R.G. Garlick, Turbine airfoil degradation in the Persian gulf war, JOM 46 (12) (1994) 39–41.
[11] F.H. Stott, D.J. de Wet, R. Taylor, Degradation of thermal-barrier coatings at very high temperature, MRS Bull. 19 (10) (1994) 46–49.
[12] M.P. Borom, C.A. Johnson, L.A. Peluso, Role of environment deposits and operating surface temperature in spallation of air plasma sprayed thermal barrier coatings, Surf. Coat. Technol. 86-87 (1996) 116–126.
[13] A.G. Evans, J.W. Hutchinson, The mechanics of coating delamination in thermal gradients, Surf. Coat. Technol. 201 (18) (2007) 7905–7916.
[14] T. Strangman, D. Raybould, A. Jameel, W. Baker, Damage mechanisms life prediction and development of EB-PVD thermal barrier coatings for turbine airfoils, Surf. Coat. Technol. 202 (4) (2007) 658–664.
[15] K.M. Grant, S. Krämer, J.P.A. Löfvander, C.G. Levi, CMAS degradation of environmental barrier coatings, Surf. Coat. Technol. 202 (4–7) (2007) 653–657.
[16] S. Krämer, J. Yang, C.G. Levi, Infiltration-inhibiting reaction of gadolinium zirconate thermal barrier coatings with CMAS melts, J. Am. Ceram. Soc. 91 (2) (2008) 576–583.
[17] S. Krämer, S. Faulhaber, M. Chambers, D.R. Clarke, C.G. Levi, J.W. Hutchinson, A.G. Evans, Mechanisms of cracking and delamination within thick thermal barrier systems in aero-engines subject to Calcium–Magnesium–Alumino-Silicate (CMAS) penetration, Mater. Sci. Eng. A 490 (1–2) (2008) 26–35.
[18] M.H. Vidal-Setif, N. Chellah, C. Rio, C. Sanchez, O. Lavigne, Calcium-magnesium-alumino-silicate(CMAS) degradation of EB-PVD thermal barrier coatings: Characterization of CMAS damage on ex-service high pressure blade TBCs, Surf. Coat. Technol. 208 (2012) 39–45.
[19] J. Wu, H.B. Guo, Y.Z. Gao, S.K. Gong, Microstructure and thermo-physical properties of yttria stabilized zirconia coatings with CMAS deposits, J. Eur. Ceram. Soc. 31 (2011) 1881–1888.
[20] F.H. Stott, D.J. de Wet, R. Taylor, The effect of molten silicate deposits on the stability of thermal barrier coatings for turbine applications at very high temperatures, 3rd International SAMPE Metals and Metals Processing Conference, Toronto, Canada October 20- October 22 1992, pp. 92–101.
[21] S. Krämer, J. Yang, C.G. Levi, Thermochemical interaction of thermal barrier coatings with molten CaO–MgO–Al_2O_3–SiO_2 (CMAS) deposits, J. Am. Ceram. Soc. 89 (10) (2006) 3167–3175.
[22] R. Wellman, G. Whitman, J.R. Nicholls, CMAS corrosion of EB-PVD TBCs: identifying the minimum level to initiate damage, Int. J. Refract. Met. Hard Mater. 28 (1) (2010) 124–132.
[23] R.T. Wu, M. Osawa, T. Yokokawa, K. Kawagishi, H. Harada, Degradation mechanisms of an advanced jet engine service-retired TBC component, J. Solid. M. Eng. 4 (2) (2010) 119–130.
[24] J. Kim, M.G. Dunn, A.J. Baran, D.P. Wade, E.L. Tremba, Deposition of volcanic materials in the hot sections of two gas turbine engines, J. Eng. Gas Turbines Power 115 (1993) 641–651.
[25] P. Mechnich, W. Braue, U. Schulz, High-temperature corrosion of EB-PVD ytttria partially stabilized zirconia thermal barrier coatings with an artificial volcanic ash overlay, J. Am. Ceram. Soc. 94 (3) (2011) 925–931.
[26] C. Mercer, S. Faulhaber, A.G. Evans, R. Darolia, A delamination mechanism for thermal barrier coatings subject to Calcium–Magnesium–Alumino-Silicate (CMAS) infiltration, Acta Mater. 53 (4) (2005) 1029–1039.
[27] X. Chen, Calcium–Magnesium–Alumina-Silicate (CMAS) delamination mechanisms in EB-PVD thermal barrier coatings, Surf. Coat. Technol. 200 (11) (2006) 3418–3427.
[28] J.M. Drexler, A.D. Gledhill, K. Shinoda, A.L. Vasiliev, K.M. Reddy, S. Sampath, N.P. Padture, Jet engine coating for resisting volcanic ash damgae, Adv. Mater. 23 (21) (2011) 2419–2424.
[29] C.G. Levi, J.W. Hutchinson, M.H. Vidal-Sétif, C.A. Johnson, Environment degradation of thermal-barrier coatings by molten deposits, MRS Bull. 37 (10) (2012) 932–941.
[30] P. Poza, J. Gómez-García, C.J. Múnez, TEM analysis of the microstructure of thermal barrier coatings after isothermal oxidation, Acta Mater. 60 (20) (2012) 7197–7206.
[31] B.J. Lecomte, F. Schuber, P.J. Ennis, New materials for advanced thermal barrier coatings, Proceedings of the 6th Liège Conference, Part III, Materials for Advanced Power Engineering, Jülich, Germany 1998, pp. 162–165.
[32] S. Sodeoka, M. Suzuki, T. Inoue, K. Ueno, S. Oki, Thermal and mechanical properties of plasma sprayed ZrO_2–CeO_2–Y_2O_3 coatings, Proceedings of the 9th National Thermal Spray Conference: Thermal Spray-Practical Solutions for Engineering Problems, ASM International, Cincinnati, Ohio 1996, pp. 295–302.
[33] C.G. Kontoyannis, M. Orkoula, Quantitative determination of the cubic,tetragonal and monoclinic phases in partially stabilized Zirconias by Raman spectroscopy, J. Mater. Sci. 29 (20) (1994) 5316–5320.
[34] A.F. Renteria, B. Saruhan, Effect of ageing on microstructure changes in EB-PVD manufactured standard PYSZ top coat of thermal barrier coatings, J. Eur. Ceram. Soc. 26 (2006) 2249–2255.
[35] D.R. Spearing, J.Y. Huang, Zircon synthesis via sintering of milled SiO_2 and ZrO_2, J. Am. Ceram. Soc. 81 (7) (1998) 1964–1966.
[36] J.M. Drexler, A. Aygun, D. Li, R. Vaßen, T. Steinke, N.P. Padture, Thermal-gradient testing of thermal barrier coatings under simultaneous attack by molten glassy deposits and its mitigation, Surf. Coat. Technol. 204 (2010) 2683–2688.
[37] N.P. Bansal, S.R. Choi, Properties of CMAS glass from desert sand, Ceram. Int. 41 (3) (2015) 3901–3909.
[38] J.M. Drexler, K. Shinoda, A.L. Ortiz, D. Li, A.L. Vasiliev, A.D. Gledhill, S. Sampath, N.P. Padture, Air-plasma-sprayed thermal barrier coating that are resistant to high-temperature attack by glassy deposits, Acta Mater. 58 (2010) 6835–6844.